

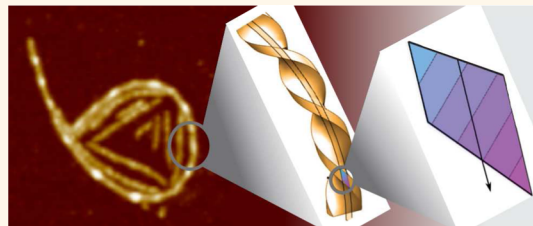
Adsorption at Liquid Interfaces Induces Amyloid Fibril Bending and Ring Formation

Sophia Jordens,[†] Emily E. Riley,^{‡,§,||} Ivan Usov,[†] Lucio Isa,^{§,||} Peter D. Olmsted,^{*,‡,#} and Raffaele Mezzenga^{*,†}

[†]Department of Health Sciences & Technology, Laboratory of Food & Soft Materials, ETH Zurich, 8092 Zurich, Switzerland, [‡]School of Physics & Astronomy, Soft Matter Physics Group, University of Leeds, Leeds LS2 9JT, United Kingdom, and [§]Department of Materials, Laboratory for Surface Science & Technology, ETH Zurich, 8093 Zurich, Switzerland. ^{||}Present address: Cambridge University, Department of Applied Mathematics and Theoretical Physics, Cambridge CB3 0WA, United Kingdom. [#]Present address: ETH Zurich, Department of Materials, Laboratory for Interfaces, Soft Matter & Assembly, 8093 Zurich, Switzerland.

^{*}Present address (for P.D.O.): Georgetown University, Department of Physics and Institute for Soft Matter Synthesis and Metrology, Washington, DC 20057, USA.

ABSTRACT Protein fibril accumulation at interfaces is an important step in many physiological processes and neurodegenerative diseases as well as in designing materials. Here we show, using β -lactoglobulin fibrils as a model, that semiflexible fibrils exposed to a surface do not possess the Gaussian distribution of curvatures characteristic for wormlike chains, but instead exhibit a spontaneous curvature, which can even lead to ring-like conformations. The long-lived presence of such rings is confirmed by atomic force microscopy, cryogenic scanning electron microscopy, and passive probe particle tracking at air– and oil–water interfaces. We reason that this spontaneous curvature is governed by structural characteristics on the molecular level and is to be expected when a chiral and polar fibril is placed in an inhomogeneous environment such as an interface. By testing β -lactoglobulin fibrils with varying average thicknesses, we conclude that fibril thickness plays a determining role in the propensity to form rings.



KEYWORDS: β -lactoglobulin · amyloid fibrils · biopolymers · interfaces · bending · statistical analysis · atomic force microscopy

Polymers exposed to an unfavorable environment can collapse or change shape in order to minimize surface energy.^{1–3} Examples of unfavorable environments include a poor solvent or a hydrophilic–hydrophobic interface like the one between water and either air or oil. Examples of conformations driven by such energy minimization are rings, loops, coils, spools, tori/toroids, hairpins or tennis rackets.⁴ In filaments comprising aggregated proteins or peptides, ring formation falls into two main classes: fully annealed rings occasionally observed as intermediate states during protein fibrillation, like in apolipoprotein C-II⁵ and $\text{A}\beta_{1-42}$,⁶ or ring formation in actively driven systems, where the energy required for filament bending is provided by GTP or ATP.^{7–10} Insulin has been shown to form open-ring shaped fibrils when pressure was applied during fibrillation,¹¹ which was explained by an anisotropic distribution of void volumes in fibrils and therefore aggregation into bent fibrils.

We study amyloid fibrils, which are linear supramolecular assemblies of proteins/peptides that, despite a large diversity in possible peptide sequences, show remarkable structural homogeneity. Peptides form β -sheets that stack, often with chiral registry, to form a filament whose main axis is perpendicular to the β -strands.^{12,13} Fully formed fibrils can consist of one or, more commonly, multiple filaments, assembled into twisted ribbons with a twist pitch determined by the number of filaments in the fibrils.¹⁴ Their high aspect ratio (diameter usually less than 10 nm, total contour length up to several μm) leads to liquid crystalline phases in both three (3D)¹⁵ and two dimensions (2D).^{16,17} Amyloid fibrils were initially studied due to their involvement in many different degenerative diseases such as diabetes II or Parkinson's disease.¹⁸ However, protein fibrils have recently experienced a surge of interest in potential applications in materials,¹⁹ and functional roles have been identified in biological processes such as hormone storage,²⁰ emphasizing

* Address correspondence to pdo7@georgetown.edu, raffaele.mezzenga@hest.ethz.ch.

Received for review July 31, 2014 and accepted October 22, 2014.

Published online October 22, 2014
10.1021/nn504249x

© 2014 American Chemical Society

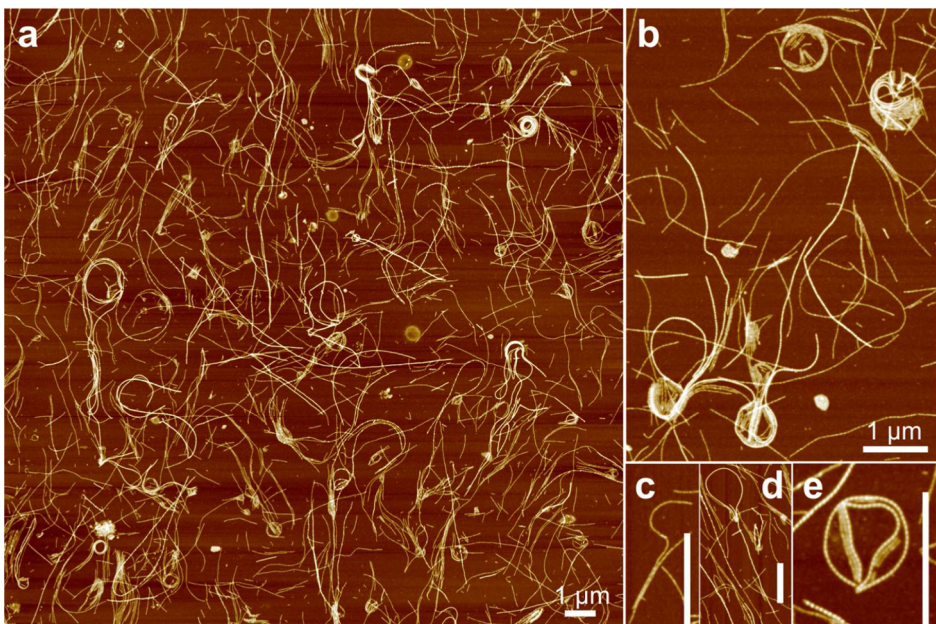


Figure 1. β -Lactoglobulin fibrils form rings and loops at the air–water interface. AFM images of β -lactoglobulin fibrils at the air–water interface after horizontal transfer onto mica using the Langmuir–Schaefer method. The initial fibril concentration in the bulk was $c_{\text{init}} = 0.001\%$ (w/w) and the waiting time before transfer $t = 60$ min. The scale bars in panels c–e correspond to $1\text{ }\mu\text{m}$.

the importance of understanding their structure and properties in 2D.

Here, we present experimental evidence for the development of *curved* fibrils at interfaces. Semiflexible β -lactoglobulin fibrils are found to undergo a shape change and passively form open rings upon adsorption to an interface (liquid–liquid or liquid–air). We show that this cannot be described by a simple bending modulus; this bending can instead be understood in terms of a *spontaneous curvature* induced on symmetry grounds by the chiral and polar nature of the fibril, when interacting with the heterogeneous environment provided by an interface. A comparison of different fibril batches of the same protein shows that the probability of forming rings depends on the average fibril thickness, with batches of thicker fibrils not forming loops. These results imply that flexible nonsymmetric bodies embedded in heterogeneous media, such as the physiological environment, can be expected to deform, bend, and twist, depending on the specific surface interaction with the environment. For example, concentration gradients of ions or pH could enhance shape changes necessary for locomotion in flexible nanoswimmers,^{21,22} or be used to promote or control self-assembly through shape changes. One could even envision high surface to volume materials such as bicontinuous phases with large length scales being used to process large amounts of flexible shape changers.

RESULTS AND DISCUSSION

Morphology. When imaging the air–water interfacial fibril layer by AFM using a modified Langmuir–Schaefer horizontal transfer technique (see Experimental Section)

to resolve 2D liquid crystallinity, we found that, in addition to nematic and isotropic fibril domains,¹⁷ some β -lactoglobulin fibrils were present in circular conformations. These rings appear at the lowest interfacial density investigated, where fibril alignment is still negligible,¹⁷ and persist in the presence of nematic fibril domains up to high densities [see Supporting Information Note 1 and Figures S1 and S2]. Ring diameters range from 0.5 to $2\text{ }\mu\text{m}$ (Figures 1 and 2), and are consistent whether observed *via* AFM at the air–water interface, cryogenic Scanning Electron Microscopy (cryo-SEM) or passive probe particle tracking at the oil–water interface, confirming that fibrils have a similar tendency to bend at air–liquid and liquid–liquid interfaces. A small selection of the vast variety of ring morphologies is presented in Figure 1. Highly complex structures involving several fibrils are quite common (Figure 1a,b, Supporting Information Figures S1 and S2), whereas relatively few distinct rings or tennis rackets comprise a single fibril and can rather be thought to be intermediate assembly states *en route* to final ring structures (Figure 1c,d).²³ Short fibrils, which could be the result of fracture due to the bending strain, exposure to air or inhomogeneous strong surface tension, also assemble into rings (Supporting Information Figure S3). Alternatively, short fibrils frequently accumulate within an outer ring and align either along the circumference of this ring or parallel to each other in the center, with minimal contact with the ring itself (Figure 1b,e).

The long-lived presence, and hence inferred stability, of these self-organized conformations was confirmed by passive probe particle tracking experiments

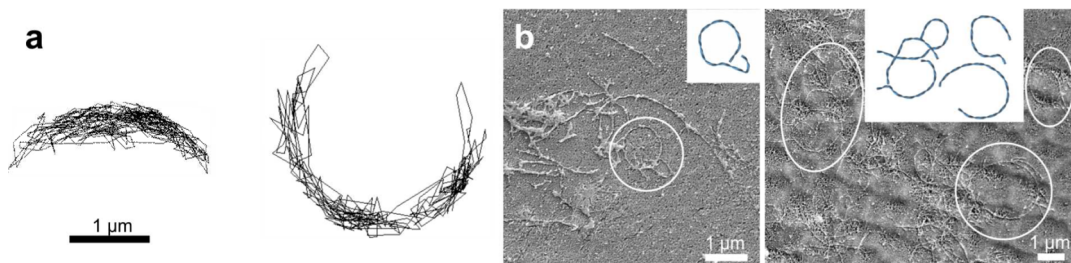


Figure 2. Fibril rings at an oil–water interface. (a) Trajectories of two different silica tracer particles with diameter ≈ 774 nm moving around circular obstacles during a passive probe particle tracking experiment of a $c_{\text{init}} = 0.005\%$ (w/w) fibril suspension. The trajectories were isolated $t = 24$ and 37 min after interface creation, respectively. The scale bar applies to both trajectories. (b) Cryo-SEM images of the surface of a $c_{\text{init}} = 0.001\%$ (w/w) fibril suspension $t = 60$ min after medium chain triglycerides (MCT)–water interface creation. The oil phase had been removed by freeze-fracture prior to imaging. Insets show sketches of the rings indicated with circles in the main images.

performed at the oil–water interface, where fluorescently labeled spherical tracer particles (diameter ≈ 774 nm) were observed to move in near-perfect circles or sickle-shaped trajectories over the course of 3–4 min. A simple pathway for ring formation could be the presence of nano- or microbubbles at the liquid surface, which give fibrils the opportunity to bend around their circumference.²⁴ This would, however, also lead to a distortion of the peptide layer (see Experimental Section) at the interface; once the sample has dried, the bubble would have disappeared but still be visible in AFM images as a height discontinuity through the “bubble”. The absence of such observations in AFM (Supporting Information Figure S4), or of bubbles (cavities) in the cryo-SEM images (Figure 2), indicates that there is an inherent predisposition of the fibrils to bend, which then leads to circle formation upon interaction with a liquid surface.

Fibril Free Energy. Understanding these data requires a study of how surface effects influence the shape of fibrils (or indeed filaments). We consider an inextensible fibril of length L , represented as a twisted ribbon with chiral wavelength λ and pitch angle θ_p given by $\cot^{-1}(2\pi R/\lambda)$, where R is the inscribing radius of the twisted ribbon (see Supporting Information Note 2). We parametrize the shape by $\hat{\mathbf{t}}(s)$, the direction parallel to the central axis of the ribbon, or equivalently the tangent vector of the fibril. The ribbon twists around its axis $\hat{\mathbf{t}}(s)$ by the angle $\phi(s)$. We will parametrize the bending in terms of the angular rate of deflection $\dot{\Theta} = \dot{\mathbf{t}} \times \hat{\mathbf{t}}$, where $\kappa(s) = d\hat{\mathbf{t}}/ds \equiv \dot{\mathbf{t}}$ is the local curvature. Hence, $\dot{\Theta} = \kappa \hat{\mathbf{n}}$, where $\hat{\mathbf{n}}$ is the axis about which the tangent vector is deflected during a bend. For a fibril confined to bend on a surface, we take $\hat{\mathbf{n}}$ to be outward surface normal vector (pointing *into* the liquid), so that κ can be either positive or negative. The free energy is given by²⁵

$$G_{\text{fib}} = \int_0^L ds \left\{ \frac{B}{2} \dot{\Theta}^2 + \frac{C}{2} (\dot{\phi} - \mathbf{q})^2 + \mathbf{D} \cdot \dot{\mathbf{t}} \times (\dot{\phi} - \mathbf{q}) \right\} \quad (1)$$

$$= \int_0^L ds \left\{ \frac{B}{2} \kappa^2 + \dots \right\} \quad (2)$$

The first term penalizes bending, where B is the bending modulus. The second term penalizes twist relative to the native helical twist, which is parametrized by the chiral wavenumber $q = 2\pi/\lambda$. Here, C is the twist modulus. The vector \mathbf{D} represents the twist-bend couplings allowed by a polar fibril with a nonsymmetric local cross section.²⁵ In this work we will focus on the bend degrees of freedom, since in filaments with free ends, such as those considered here, the twist degrees of freedom will relax to accommodate any imposed bend.

A polar twisted fibril has an anisotropy that distinguishes “head” from “tail” directions along the fibril axis; in F-actin this “polarization” arises from the orientations required of G-actin monomers to effect self-assembly,²⁶ in an α -helix the N–C polymerization breaks the polar symmetry and in cross- β amyloid fibrils such as those studied here the polarity is due to the molecular packing of β -sheets.^{27–29} The polarity is reflected in variations in molecular structure along the exposed surface of the twisted ribbon. When this structure is placed in a heterogeneous environment, as occurs near a solid surface or when immersed within a meniscus between two fluids (or fluid and gas), the inhomogeneity of the environment generally leads to unbalanced torques on the body (see Supporting Information Note 2, Figures S5 and S6 for details), even when local forces have balanced to place the fibril at the interface. A nonsymmetric body, such as a chiral and polar fibril, can thus experience an effective spontaneous curvature.³⁰

To demonstrate this effect, we consider a fibril adsorbed onto a planar surface with which it interacts, rather than immersed *within* a meniscus. The effects are qualitatively the same, but the details are easier to understand in the adsorbed case. The surface and the adsorbed ribbon interact *via* numerous molecular interactions.³¹ Although in principle *all* atoms in the fibril interact with every point on the surface due to Coulomb interactions, screening limits the interaction to only the adsorbing surface. Long-range dispersion interactions are also irrelevant for fibrils that are

induced to bend or twist within the plane, since the change in this energy will be negligible. Hence, we consider the following surface free energy

$$G_{\text{surf}} = \frac{2L}{\lambda} \int_S [\bar{\gamma} + \delta\gamma(\mathbf{r})] d^2r \quad (3)$$

where λ is the twist pitch or wavelength, the average surface energy $\bar{\gamma}$ controls adsorption, and S is the contact area of a the ribbon, which occurs every half wavelength. The asymmetry $\delta\gamma(\mathbf{r})$ reflects the polar nature of the interaction and can vary from repulsive to attractive along the repeat patch. A polar moment (with dimensions of energy) of the interaction can be defined by

$$\mathbf{P} = \frac{2}{\lambda} \int_S \mathbf{r} \delta\gamma(\mathbf{r}) d^2r \quad (4)$$

where S is the area of the patch where the fibril contacts the surface. The polar moment \mathbf{P} is determined by the nature of the interaction with the surface, and is thus not an intrinsic property of the fibril alone. Figure 3 shows an example in which the surface patch is a parallelogram with length ℓ and width ω . For a simple surface potential $\delta\gamma(\mathbf{r}) = \varepsilon(x \cos \Phi + y \sin \Phi)$, where the coordinate x is parallel to the fibril axis coordinate s , the polar moment (see Supporting Information Note 2) has magnitude $P = \alpha(\theta_p, \Phi) \omega^3 / \varepsilon \lambda$. Here, $\alpha(\theta_p, \Phi)$ is a geometric prefactor whose sign depends on the polarization and chirality, and parametrizes the degree to which the symmetric parallelogram is deformed into a nonsymmetric shape to favor one sign of surface “charge”.

When the twisted ribbon is bent the ribbon-surface contact area changes shape, so that either the repulsive or attractive part of the polar interaction has more contact with the surface, depending on the sign of the bend (Figure 3c). This leads to a spontaneous curvature. The contribution of bending to the overall interaction energy can then be written as a chiral coupling between the bending rate $\dot{\Theta}$ and the polar moment \mathbf{P} :

$$G_{\text{surf}} = \int_0^L ds \{ -A\dot{\Theta} \cdot \hat{\mathbf{t}} \times \mathbf{P} + \dots \} \quad (5)$$

$$= \int_0^L ds \{ -A\kappa \hat{\mathbf{n}} \cdot \hat{\mathbf{t}} \times \mathbf{P} + \dots \} \quad (6)$$

The vector product is the simplest term which has no mirror symmetry, and is thus appropriate for a chiral filament. Moreover, under $s \rightarrow -s$ both κ and \mathbf{t} change sign, whereas \mathbf{P} does not, so that the free energy is also reparametrization-invariant. The dimensionless geometric factor A and the moment \mathbf{P} depend on the details of the surface free energy $\delta\gamma(\mathbf{r})$ interaction potential U , the contact area shape, and its deformation under bending. The polar moment \mathbf{P} depends on the surface normal vector through its vector nature and the details of the surface–fibril interaction. The

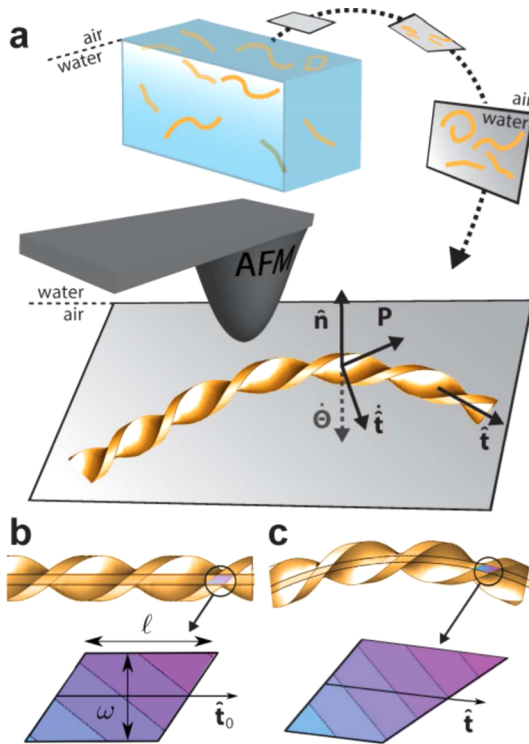


Figure 3. Twisted ribbon against a surface. (a) After horizontal transfer of the interfacial fibril layer, the AFM tip probes the fibrils from the side that was originally pointing toward the water phase. (b and c) The contact area as seen through the interface from the air-side is a parallelogram (b), which deforms asymmetrically when the fibril is bent (c). This leads to a greater contact area by one ‘charge’ (indicated by color) of the polar interaction, which implies a preference for one sign of bend and thus a spontaneous curvature. The example shown is that of a bend that decreases the contact energy. The symmetry breaking of the polar region upon bending has been amplified for visualization purposes.

ellipses indicate other terms induced by the surface, such as contributions to the bend-twist or curvature moduli, or a spontaneous twist. We choose the convention that the surface normal vector $\hat{\mathbf{n}}$ points away from the surface and thus into the fibril. An example free energy $G_{\text{fib},P}$ is calculated in the Supporting Information for a simple model contact potential.

The curvature in eq 6 carries a sign: for $\kappa > 0$, the fibril bends in a right-handed sense around the surface normal vector $\hat{\mathbf{n}}$, while for $\kappa < 0$, the fibril bends in a left-handed sense. The process of transferring the surface layer for AFM observation orients the surface normal toward the AFM observer, so that observation is from the liquid side toward the air side (Figure 3). Consider a polarization such that $\mathbf{P} \cdot \hat{\mathbf{y}} = \sin \Phi$, where $\Phi = +\pi/4$, and choose $\hat{\mathbf{t}} \parallel \hat{\mathbf{x}}$ (as observed in the AFM image; see Figure 3), where $\hat{\mathbf{x}} \times \hat{\mathbf{y}} = \hat{\mathbf{n}}$. This implies $\hat{\mathbf{n}} \cdot \hat{\mathbf{t}} \times \mathbf{P} > 0$. Consider a bend as shown in Figure 3, in which $\dot{\Theta} \cdot \hat{\mathbf{n}} = \kappa$, where $\kappa < 0$. In Supporting Information Note 2 we find $A > 0$, so that this bend ($\kappa < 0$) increases the energy, and thus $\kappa > 0$ is favored. Similarly, for the opposite sign of $\hat{\mathbf{t}} \times \mathbf{P}$, a negative curvature $\kappa < 0$ is favored.

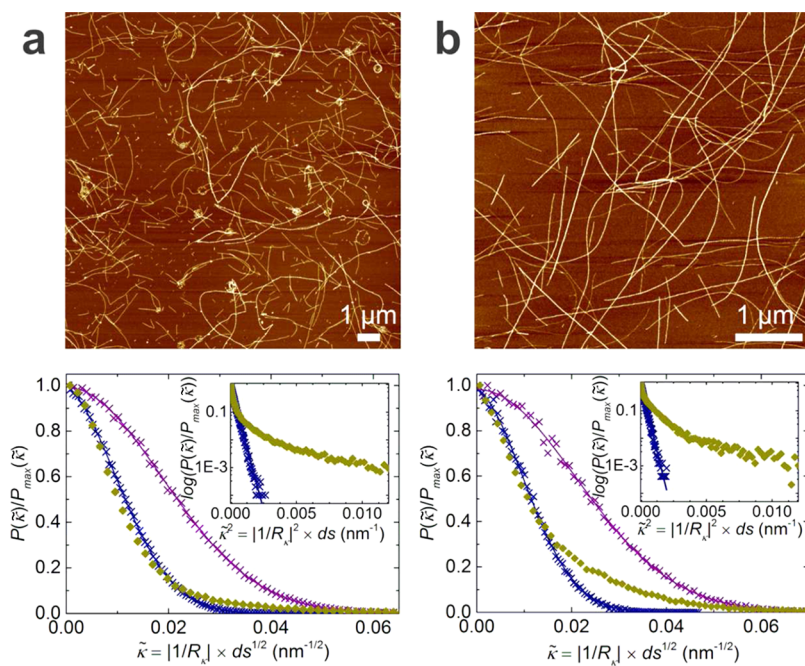


Figure 4. Fibrils exhibit a spontaneous curvature when adsorbed to a surface. (Upper panel) Zoomed in images of β -lactoglobulin fibrils (a) at the air–water interface after $t = 10$ min of adsorption from a $c_{\text{init}} = 0.001\%$ (w/w) fibril suspension and (b) deposited onto mica for 2 min from the bulk with $c_{\text{init}} = 0.1\%$ (w/w). (Lower panel) Probability distributions of normalized absolute local curvatures κ extracted from the full (a) $30 \times 30 \mu\text{m}$ (see Supporting Information for full image) and (b) $5 \times 5 \mu\text{m}$ images (green diamonds) with a ds of 24 and 9.8 nm, respectively. The curvature distribution of simulated WLCs generated using all relevant parameters from the corresponding AFM image (see Experimental Section) is shown as purple crosses and is successfully fitted with a Gaussian probability distribution function (purple line). Tracking these WLCs results in a change in the probability densities (blue crosses) but the values are still Gaussianly distributed (blue line). Plotting the normalized probabilities in logarithmic scale as a function of κ^2 clearly shows fat tails and, thus, the presence of spontaneous curvature only in real fibrils (insets in the lower panels).

The competition between the surface energy eq 6 and the ordinary fibril bending energy eq 1 leads, by minimization, to a spontaneous curvature κ_0 given by (see Supporting Information)

$$\kappa_0 = \frac{A}{B} \hat{\mathbf{n}} \cdot \hat{\mathbf{t}} \times \mathbf{P} \quad (7)$$

This is equal to $\varepsilon\omega^3/\alpha(\theta_p, \Phi)/B\lambda \sin^2 \theta_p$ for the simple surface potential $\delta\gamma(\mathbf{r}) = \varepsilon(x \cos \Phi + y \sin \Phi)$. Isambert and Maggs³⁰ articulated how a surface can induce spontaneous curvature in a polar and chiral filament. They proposed a phenomenological free energy with an explicit spontaneous curvature that depends on the twist angle, and a surface interaction that breaks polar symmetry. Hence, they have actually introduced a spontaneous curvature “by hand”. Conversely, we present a model in which a polar surface interaction is itself chiral by virtue of the local chirality of the filament, and this gives rise to an effective spontaneous curvature as a result of total energy minimization. Therefore, the functional form of the resulting spontaneous curvature differs from that proposed in ref 30.

Enhanced curvature is expected for amyloid fibrils with fewer filaments (as confirmed in Figure 5), which will have smaller bending moduli B , or for fibrils with larger polar moments P and thus stronger surface interactions. In addition, the specific details of the

surface deformation encapsulated in the function $\alpha(\theta_p, \Phi)$ play an important role: fibrils for which the deformation leads to a more symmetric contact area will have a stronger geometric factor and thus a greater expected spontaneous curvature.

Non-Gaussian Curvature Distributions. Consider a segment of arc length ds of a wormlike chain (WLC). The probability $\mathcal{P}(\kappa)$ of finding this segment curved with curvature $\kappa = 1/R_\kappa$, where R_κ is the radius of curvature, is governed by the bending modulus and should be Gaussianly distributed, $\mathcal{P}(\kappa) \sim \exp\{-ds/\kappa_p^2/2\}$, where $\kappa_p = B/k_B T$ is the persistence length. Deviations from the WLC model can be quite common, as with toroidal DNA,^{32,33} in which the nucleic acids have a smaller persistence length at short length scales.³² The presence of rings in our system suggests a characteristic intrinsic curvature or length scale, in addition to the usual κ_p . For quantitative analysis, we have extracted the xy coordinates of fibrils from images acquired at low interfacial fibril densities after short adsorption times, where interactions and contact between fibrils are still minimal, and calculated $\mathcal{P}(\kappa)$ (Figure 4; see Materials and Methods). Any rings present on the image were excluded from the analysis, since their closed topology would introduce an additional constraint. To benchmark this approach, we first generate conformations based on the discrete WLC

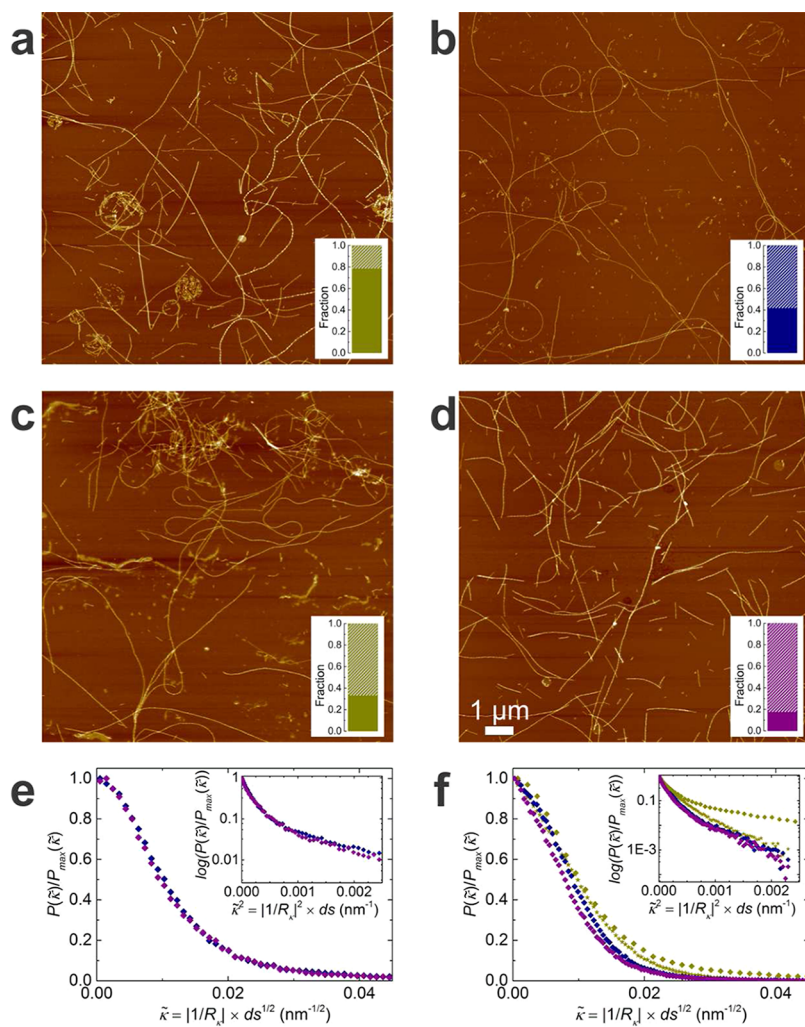


Figure 5. Fibril thickness affects probability of observing rings at the air–water interface. (a–d) Fraction of double- (solid bar) and triple-stranded fibrils (striped bar) in batches of fibrils formed from three different suppliers. Data correspond to the ratio of the area under each of the two peaks to the total area of the average height per fibril distribution obtained on AFM samples of fibrils at the air–fibril solution interface with $c_{\text{init}} = 0.001\%$ (w/w). Rings are observed most frequently in batch 1 from source 1 (a), looped structures are found in fibrils from source 2 (b), and batch 2 from source 1 (c), whereas fibrils from source 3 do not form rings (d). The scale bar applies to all AFM images. (e) Probability distributions of normalized absolute local curvatures κ for only double- (blue diamonds) and only triple-stranded fibrils (purple diamonds) for the sample shown in a and Figure 4a. Less spontaneous curvature is found for thicker fibrils (inset). (f) Probability distributions of normalized absolute local curvatures $\tilde{\kappa}$ for the samples shown in a (green diamonds), b (blue diamonds), c (green stars), and d (purple diamonds). Samples with higher fractions of thicker fibrils have less pronounced fat tails in their normalized $\mathcal{P}(\kappa)$ distribution (inset).

model with the ℓ_p obtained from the 2D mean squared end-to-end distance of fibrils at the air–water interface.³⁴ These conformations are used to create artificial images of WLC polymers with the same resolution as the AFM images and then subjected to the same tracking algorithm used for analyzing the real fibril image. Figure 4 shows the normalized probability distribution of curvatures $\mathcal{P}(\kappa)/\mathcal{P}_{\text{max}}(\kappa)$ for both the original WLCs and the corresponding tracked conformations (see Experimental Section). In the tracked conformations the distribution shifts toward lower curvatures: this change is due to finite image resolution (Figure 4a). Importantly, however, both distributions are Gaussian. In contrast, and as expected from the theoretical considerations put forth above, the

normalized $\mathcal{P}(\kappa)$ for real fibrils adsorbed at the air–water interface can indeed not be fitted with a single Gaussian distribution function but has a pronounced fat tail instead.

It has been argued that differences in κ_0 are to be expected depending on the strength of adsorption to the surface³⁵ and on whether the polymer is in 3D or 2D.³⁶ To test this, we compare the curvature distributions from fibrils adsorbed to the air–water interface and transferred horizontally to mica (Figure 4a) to fibrils deposited onto mica from a drop of the bulk solution (Figure 4b). The modified Langmuir–Schaefer AFM sample preparation is a 2D to 2D transfer from a liquid onto a solid surface, which is much faster (milliseconds) than the slower (seconds) 3D to 2D

equilibration obtained by depositing onto a solid substrate from bulk.³⁴ The bending probability of fibrils adsorbed from the bulk to mica, where no rings are observed, was also found to deviate from a typical Gaussian distribution (Figure 4b). Fibrils, hence, bend as a result of their exposure to the inhomogeneous environment of solid–liquid, liquid–liquid, and gas–liquid interfaces, independently of how they initially adsorbed at these phase boundaries.

Average Fibril Thickness Determines Propensity to Bend. As noted above, we predict a larger fibrillar diameter to imply a larger bending modulus, and hence a smaller likelihood of bending spontaneously (according to eq 7). This was confirmed by studying fibrils from different batches of preparation, as well as from different suppliers. Figure 5 shows ratios of double- to triple-stranded fibrils for β -lactoglobulin fibrils produced from native protein obtained from three different suppliers. Nonidentical distributions can be expected due to different fibril processing conditions (sample volumes, shearing and stirring histories) between batches, and/or genetic variants between suppliers.³⁷ This then affects the individual filament thickness, and number of filaments per fibril, due to subtle differences in proteolysis. Thicker filaments, with larger bending moduli, should have much smaller spontaneous curvatures, and not be visibly curved if thick enough. Figure 5 shows the distribution of number of strands per fibril, which is proportional to thickness, as determined from the AFM images. The batch with the highest number of rings (Figure 1) contains the largest amount of double-stranded fibrils (Figure 5a). By contrast, for batches of fibrils formed with the same protocol but from protein obtained from a different supplier, primarily three-stranded fibrils were found, which did not assemble into rings (Figure 5d). Both a second batch of fibrils from the first source as well as a batch from a third supplier containing a more even mix of double- and triple-stranded fibrils yielded curved conformations (Figure 5b and c). By separating the data used to calculate the normalized distribution of $\mathcal{P}(\kappa)$ presented in Figure 4a into double- and triple-stranded fibrils (Figure 5e), we confirm that the normalized $\mathcal{P}(\kappa)$ distribution of thick fibrils has a less pronounced fat tail and these fibrils thus bend less than their thinner counterparts. A similar trend is observed for the different batches in Figure 5a–d, where a

higher fraction of thicker fibrils in the sample results in less curved structures at the air–water interface and less spontaneous curvature (Figure 5f).

CONCLUSIONS

We provide evidence from three different and independent experimental techniques for the presence of complex self-assembled amyloid fibril structures at air–water and oil–water interfaces. It has previously been reported that fibril ends are particularly reactive, as shown in the disruption of liposomes occurring preferentially at fibril ends.³⁸ Their enhanced fibrillation properties as compared to the rest of the fibrils^{39–42} in addition to possible capillary interactions⁴³ may play a role in the observed tendency of fibrils to form almost-closed rings. The genesis of these rings and loops is explained by a spontaneous curvature arising from the interaction of polar, chiral and semiflexible fibrils with an interface. Because a spontaneous curvature but no ring formation was determined in fibrils at the solid mica–liquid interface, it can be concluded that a certain degree of mobility at the interface supports the assembly of fibrils into such geometries. This is in agreement with the fact that amyloid fibrils adsorbed onto a mica surface from bulk can asymptotically reach the expected 3/4 exponent for a self-avoiding random walk in 2D.^{44,45} The ability of fibrils to form rings correlates with the average fibril height distribution, with loops only observed in systems where single- and double-stranded fibrils dominate. A shift in fibril height toward more triple-stranded populations reduces the number of high curvature counts and thus the amount of ring structures present. It is noteworthy, however, that a spontaneous curvature is expected also for thicker fibrils but at lower κ because of their higher bending modulus, meaning that only thick fibrils which are long enough ($L \geq 2\pi/\kappa$) will be able to form full rings. These findings have consequences for the understanding of how fibrils deposit *in vivo*, the morphology of plaques, biomechanical interactions of chiral filaments with surrounding tissues, and ultimately their effect on cells and organisms. A larger natural dynamic analogue in the form of the circular motion of polarly flagellated bacteria near solid surfaces has been described in the literature,⁴⁶ and together, these results could be seen as a new approach for the controlled design, fabrication or improvement of nanoswimmers and -robots.

EXPERIMENTAL SECTION

Fibril Formation. Amyloid β -lactoglobulin fibrils were prepared according to the protocol of Jung *et al.*¹⁵ The native, freeze-dried protein was obtained from three different sources: Davisco, Sigma, and TU Munich.⁴⁷ A 2% (w/w) solution of purified and dialyzed β -lactoglobulin was stirred for 5 h at 90 °C and pH 2. The resultant fibrils were then dialyzed against pH 2 Milli-Q water for 5–7 days to remove unconverted

proteinaceous material. There is, however, evidence that even after complete removal of nonfibrillar material, the system will go back to an equilibrium point where both fibrils and “free” peptides are present. This has been proposed for the case of $\text{A}\beta_{1-40}$ and SH3 domain fibrils^{40,48} and recently for β -lactoglobulin.^{17,49} Another pathway for the accumulation of peptides may be the disaggregation of fibrils upon adsorption to the air–water interface.

Atomic Force Microscopy. Sample preparation and atomic force microscopy (AFM) were performed as described previously.¹⁷ All samples contained no added salt. For the modified Langmuir–Schaefer technique, a 2 μL aliquot of a fibril solution of desired concentration c_{init} was carefully pipetted into a small glass vial and left to stand for time t . For a given c_{init} , the interfacial fibril density increases with t as more fibrils adsorb to the interface. A freshly cleaved mica sheet glued to a metal support was lowered toward the liquid surface horizontally and retracted again immediately after a brief contact. The mica was then dipped into ethanol ($\geq 99.8\%$ v/v) to remove any unadsorbed bulk material before drying the sample under a weak clean air flow. Alternatively, images of fibrils in the bulk were collected by pipetting 20 μL of the sample onto a freshly cleaved mica. After 2 min, the mica was gently rinsed with Milli-Q water and dried with pressurized air. Sample scanning in air was performed on a Nanoscope VII Multimode Scanning Probe Microscope (Veeco Instruments) in tapping mode.

Passive Probe Particle Tracking. A volume of 15 μL of a $c_{\text{init}} = 0.001\%$ (w/w) fibril sample seeded with 0.075% (w/v) fluorescein isothiocyanate labeled, positively charged silica tracer particles of diameter $\approx 774\text{ nm}$ was pipetted into an epoxy resin well on a thoroughly cleaned and plasma-treated glass coverslide. Medium chain triglycerides were poured on top so as to create a flat oil–water interface. The motion of tracers trapped at this interface was then recorded on an inverted microscope (Leica DM16000B) equipped with a 63 \times 1.4 NA oil HCX PlanApo DIC objective for up to 700 frames at a rate of 0.374 s. Images were analyzed with standard as well as custom-written software in IDL (ITT Visual Information Solutions)^{16,17,50}

Cryogenic Scanning Electron Microscopy. Samples for freeze-fracture cryogenic Scanning Electron Microscopy (FrScA cryo-SEM⁵¹) were prepared by creating a flat medium chain triglycerides (MCT)–fibril solution interface in clean, small copper holders. The fibril solution contained the same concentration of fluorescent tracer particle as in passive probe particle tracking experiments and were added here for easier location of the interface during imaging. The samples were then frozen at a cooling rate of 30 000 K s⁻¹ in a liquid propane jet freezer (Bal-Tec/Leica JFD 030) and fractured under high vacuum at $-140\text{ }^{\circ}\text{C}$ (Bal-Tec/Leica BAF060). After partial freeze-drying at $-110\text{ }^{\circ}\text{C}$ for 3 min to remove ice crystals and condensed water from the sample surfaces, they were coated with a 2 nm thin layer of tungsten at $-120\text{ }^{\circ}\text{C}$. All samples were transferred to the precooled cryo-SEM (Zeiss Gemini 1530) under high vacuum ($\approx 5 \times 10^{-7}$ mbar) with an air-lock shuttle. Imaging was performed at $-120\text{ }^{\circ}\text{C}$ with a secondary electron detector.

Local Curvature Determination. A home-built fibril tracking routine based on open active contours³⁴ was used to extract the fibrils' xy coordinates from AFM images with a tracking step length $\Delta s \approx 1$ pixel between two subsequent points along a tracked fibril. Any fibrils involved in ring formation as well as those deposited from the subphase (for example, the bright ones running from top left to bottom right of the image in Supporting Information Figure S7) were discarded from the analysis. The absolute local curvature $\kappa = |1/R_{\kappa}|$, with R_{κ} being the radius of curvature between two vectors \mathbf{v}_1 and \mathbf{v}_2 of equal length along the fibril contour with a distance ds between them, was calculated for all fibril segment pairs in the image of interest. The curvature is given by $1/R_{\kappa} = (\mathbf{v}_2(s+ds) - \mathbf{v}_1(s))/|\mathbf{v}_1|ds$, where we chose $ds = 2\Delta s$. For a fibril penalized by only a bending energy, the probability of a curved segment is given by

$$\mathcal{P}(\kappa) = \mathcal{N} e^{-(1/2)\kappa^2 ds} \quad (8)$$

where \mathcal{N} is a normalization factor, and $\kappa_p = B/k_B T$ is the persistence length.² The distribution depends on the segment length ds chosen for the calculation of bending. Of course, the intrinsic persistence length is a material property and cannot depend on this discretization. Hence, the distribution of the quantity $\tilde{\kappa} = \kappa(ds^{1/2})$ is independent of the image resolution, and was used to parametrize the distribution of curvatures.

Images of WLCs were generated using the following parameters obtained from real AFM fibril images:

1. the mean and variance of the length distribution,
2. the average fibril radius,

3. the number of fibrils per image,
4. κ_p determined from the fit of the average 2D mean squared end-to-end distance

$$\langle R_{2D}^2 \rangle = 4L_c/\kappa_p \left[1 - 2\frac{\kappa_p}{L_c} (1 - e^{-L_c/2\kappa_p}) \right] \quad (9)$$

where L_c is the internal contour length,

5. fibril tracking step Δs ,

6. and discretization ds .

The WLC coordinates from which the artificial images were created were used as such for the calculation of $\mathcal{P}(\kappa)$. Additionally, the generated chains were tracked with the same algorithm used for real AFM images to illustrate the change in $\mathcal{P}(\kappa)$ due to resolution limits in the imaging and the apparently lower but purely Gaussian curvature distribution in tracked WLCs compared to untracked WLCs.

To calculate the curvature distribution for either double- or triple-stranded fibrils, the tracked fibril data set was separated into two based on a cutoff height obtained from the average fibril height histogram.

Conflict of Interest: The authors declare no competing financial interest.

Acknowledgment. Support by the Electron Microscopy of ETH Zurich (EMEZ) is acknowledged and the authors thank A. Schofield for the silica tracers. L. Böni is thanked for his help with figure design. The authors acknowledge financial support for S.J. from ETH Zurich (ETHIIRA TH 32-1), I.U. from SNF (2-77002-11), P.D.O. from an SNSF visiting fellowship (IZK072_141955), and L.I. from SNSF grants PP00P2_144646/1 and PZ00P2_142532/1.

Supporting Information Available: Details of the free energy calculation and additional AFM images. This material is available free of charge via the Internet at <http://pubs.acs.org/>.

REFERENCES AND NOTES

1. deGennes, P.-G. *Scaling Concepts in Polymer Physics*; Cornell University Press: Ithaca, NY, 1979.
2. Doi, M.; Edwards, S. F. *The Theory of Polymer Dynamics*; Clarendon Press: Oxford, 1988.
3. Pereira, G. G. Charged, Semi-Flexible Polymers under Incompatible Solvent Conditions. *Curr. Appl. Phys.* **2008**, *8*, 347–350.
4. Cohen, A. E.; Mahadevan, L. Kinks, Rings, and Rackets in Filamentous Structures. *Proc. Natl. Acad. Sci. U.S.A.* **2003**, *100*, 12141–12146.
5. Hatters, D. M.; MacPhee, C. E.; Lawrence, L. J.; Sawyer, W. H.; Howlett, G. J. Human Apolipoprotein C-II Forms Twisted Amyloid Ribbons and Closed Loops. *Biochemistry* **2000**, *39*, 8276–8283.
6. Mustata, G.-M.; Shekhawat, G. S.; Lambert, M. P.; Viola, K. L.; Velasco, P. T.; Klein, W. L.; Dravid, V. P. Insights into the Mechanism of Alzheimer's β -Amyloid Aggregation as a Function of Concentration by Using Atomic Force Microscopy. *Appl. Phys. Lett.* **2012**, *100*, 133704-1–133704-4.
7. Paez, A.; Tarazona, P.; Mateos-Gil, P.; Vélez, M. Self-Organization of Curved Living Polymers: FtsZ Protein Filaments. *Soft Matter* **2009**, *5*, 2625–2637.
8. Tang, J. X.; Käs, J. A.; Shah, J. V.; Janmey, P. A. Counterion-Induced Actin Ring Formation. *Eur. Biophys. J.* **2001**, *30*, 477–484.
9. Kabir, A. M. R.; Wada, S.; Inoue, D.; Tamura, Y.; Kajihara, T.; Mayama, H.; Sada, K.; Kakugo, A.; Gong, J. P. Formation of Ring-Shaped Assembly of Microtubules with a Narrow Size Distribution at an Air–Buffer Interface. *Soft Matter* **2012**, *8*, 10863–10867.
10. Sumino, Y.; Nagai, K. H.; Shitaka, Y.; Tanaka, D.; Yoshikawa, K.; Chaté, H.; Oiwa, K. Large-Scale Vortex Lattice Emerging from Collectively Moving Microtubules. *Nature* **2012**, *483*, 448–452.
11. Jansen, R.; Grudzielanek, S.; Dzwolak, W.; Winter, R. High Pressure Promotes Circularly Shaped Insulin Amyloid. *J. Mol. Biol.* **2004**, *338*, 203–206.

12. Dobson, C. The Structural Basis of Protein Folding and Its Links with Human Disease. *Philos. Trans. R. Soc. London, Ser. B* **2001**, *356*, 133–145.
13. Eichner, T.; Radford, S. E. A Diversity of Assembly Mechanisms of a Generic Amyloid Fold. *Mol. Cell* **2011**, *43*, 8–18.
14. Adamcik, J.; Jung, J.-M.; Flakowski, J.; De Los Rios, P.; Dietler, G.; Mezzenga, R. Understanding Amyloid Aggregation by Statistical Analysis of Atomic Force Microscopy Images. *Nat. Nanotechnol.* **2010**, *5*, 423–428.
15. Jung, J.-M.; Mezzenga, R. Liquid Crystalline Phase Behavior of Protein Fibers in Water: Experiments *versus* Theory. *Langmuir* **2010**, *26*, 504–514.
16. Isa, L.; Jung, J.-M.; Mezzenga, R. Unravelling Adsorption and Alignment of Amyloid Fibrils at Interfaces by Probe Particle Tracking. *Soft Matter* **2011**, *7*, 8127–8134.
17. Jordens, S.; Isa, L.; Usov, I.; Mezzenga, R. Non-Equilibrium Nature of Two-Dimensional Isotropic and Nematic Coexistence in Amyloid Fibrils at Liquid Interfaces. *Nat. Commun.* **2013**, *4*, 1917–1917–8.
18. Dobson, C. M. Protein Folding and Misfolding. *Nature* **2003**, *426*, 884–890.
19. Mankar, S.; Anoop, A.; Sen, S.; Maji, S. K. Nanomaterials: Amyloids Reflect Their Brighter Side. *Nano Rev.* **2011**, *2*, 6032.
20. Maji, S. K.; Perrin, M. H.; Sawaya, M. R.; Jessberger, S.; Vadodaria, K.; Rissman, R. A.; Singru, P. S.; Nilsson, K. P. R.; Simon, R.; Schubert, D.; *et al.* Functional Amyloids as Natural Storage of Peptide Hormones in Pituitary Secretory Granules. *Science* **2009**, *325*, 328–332.
21. Sengupta, S.; Ibele, M. E.; Sen, A. Fantastic Voyage: Designing Self-Powered Nanorobots. *Angew. Chem., Int. Ed.* **2012**, *51*, 8434–8445.
22. Keaveny, E. E.; Walker, S. W.; Shelley, M. J. Optimization of Chiral Structures for Microscale Propulsion. *Nano Lett.* **2013**, *13*, 531–537.
23. Schnurr, B.; Gittes, F.; MacKintosh, F. C. Metastable Intermediates in the Condensation of Semiflexible Polymers. *Phys. Rev. E* **2002**, *65*, 061904–1–061904–13.
24. Martel, R.; Shea, H. R.; Avouris, P. Rings of Single-Walled Carbon Nanotubes. *Nature* **1999**, *398*, 299.
25. Marko, J. F.; Siggia, E. D. Bending and Twisting Elasticity of DNA. *Macromolecules* **1994**, *27*, 981–988.
26. Howard, J. *Mechanics of Motor Proteins and the Cytoskeleton*; Sinauer Associates: Sunderland, MA, 2001.
27. Rogers, S. S.; Venema, P.; van der Ploeg, J. P. M.; van der Linden, E.; Sagis, L. M. C.; Donald, A. M. Investigating the Permanent Electric Dipole Moment of β -Lactoglobulin Fibrils, Using Transient Electric Birefringence. *Biopolymers* **2006**, *82*, 241–252.
28. Fitzpatrick, A. W. P.; Debelouchina, G. T.; Bayro, M. J.; Clare, D. K.; Caporini, M. A.; Bajaj, V. S.; Jaroniec, C. P.; Wang, L.; Ladizhansky, V.; Mäller, S. A.; *et al.* Atomic Structure and Hierarchical Assembly of a Cross- β Amyloid Fibril. *Proc. Natl. Acad. Sci. U.S.A.* **2013**, *110*, 5468–5473.
29. Cohen, S. I. A.; Linse, S.; Luheshi, L. M.; Hellstrand, E.; White, D. A.; Rajah, L.; Otzen, D. E.; Vendruscolo, M.; Dobson, C. M.; Knowles, T. P. Proliferation of Amyloid- β 42 Aggregates Occurs through a Secondary Nucleation Mechanism. *Proc. Natl. Acad. Sci. U.S.A.* **2013**, *110*, 9758–9763.
30. Isambert, H.; Maggs, A. C. Bending of Actin Filaments. *Europhys. Lett.* **1995**, *31*, 263–267.
31. Israelachvili, J. N. *Intermolecular and Surface Forces*; Academic Press: London, 1992.
32. Noy, A.; Golestanian, R. Length Scale Dependence of DNA Mechanical Properties. *Phys. Rev. Lett.* **2012**, *109*, 228101–228101–5.
33. Seaton, D. T.; Schnabel, S.; Landau, D. P.; Bachmann, M. From Flexible to Stiff: Systematic Analysis of Structural Phases for Single Semiflexible Polymers. *Phys. Rev. Lett.* **2013**, *110*, 028103–1–028103–5.
34. Rivetti, C.; Guthold, M.; Bustamante, C. Scanning Force Microscopy of DNA Deposited onto Mica: Equilibration *versus* Kinetic Trapping Studied by Statistical Polymer Chain Analysis. *J. Mol. Biol.* **1996**, *264*, 919–932.
35. Joanicot, M.; Revet, B. DNA Conformational Studies from Electron Microscopy. I. Excluded Volume Effect and Structure Dimensionality. *Biopolymers* **1987**, *26*, 315–326.
36. Rappaport, S. M.; Medalion, S.; Rabin, Y. Curvature Distribution of Worm-like Chains in Two and Three Dimensions. Preprint archive at <arXiv:0801.3183> **2008**.
37. Qin, B. Y.; Bewley, M. C.; Creamer, L. K.; Baker, E. N.; Jameson, G. B. Functional Implications of Structural Differences between Variants A and B of Bovine β -Lactoglobulin. *Protein Sci.* **1999**, *8*, 75–83.
38. Milanesi, L.; Sheynis, T.; Xue, W. F.; Orlova, E. V.; Hellewell, A. L.; Jelinek, R.; Hewitt, E. W.; Radford, S. E.; Saibil, H. R. Direct Three-Dimensional Visualization of Membrane Disruption by Amyloid Fibrils. *Proc. Natl. Acad. Sci. U.S.A.* **2012**, *109*, 20455–20460.
39. Tyedmers, J.; Treusch, S.; Dong, J.; McCaffery, J. M.; Bevis, B.; Lindquist, S. Prion Induction Involves an Ancient System for the Sequestration of Aggregated Proteins and Heritable Changes in Prion Fragmentation. *Proc. Natl. Acad. Sci. U.S.A.* **2010**, *107*, 8633–8638.
40. Carulla, N.; Caddy, G. L.; Hall, D. R.; Zurdo, J.; Gairí, M.; Feliz, M.; Giralt, E.; Robinson, C. V.; Dobson, C. M. Molecular Recycling within Amyloid Fibrils. *Nature* **2005**, *436*, 554–558.
41. Knowles, T. P. J.; Waudby, C. A.; Devlin, G. L.; Cohen, S. I. A.; Aguzzi, A.; Vendruscolo, M.; Terentjev, E. M.; Welland, M. E.; Dobson, C. M. An Analytical Solution to the Kinetics of Breakable Filament Assembly. *Science* **2009**, *326*, 1533–1537.
42. Xue, W.-F.; Homans, S. W.; Radford, S. E. Systematic Analysis of Nucleation-Dependent Polymerization Reveals New Insights into the Mechanism of Amyloid Self-Assembly. *Proc. Natl. Acad. Sci. U.S.A.* **2008**, *105*, 8926–8931.
43. Botto, L.; Yao, L.; Leheny, R. L.; Stebe, K. J. Capillary Bond between Rod-Like Particles and the Micromechanics of Particle-Laden Interfaces. *Soft Matter* **2012**, *8*, 4971–4979.
44. Lara, C.; Usov, I.; Adamcik, J.; Mezzenga, R. Sub-Persistence-Length Complex Scaling Behavior in Lysozyme Amyloid Fibrils. *Phys. Rev. Lett.* **2011**, *107*, 238101–1–238101–5.
45. Usov, I.; Adamcik, J.; Mezzenga, R. Polymorphism Complexity and Handedness Inversion in Serum Albumin Amyloid Fibrils. *ACS Nano* **2013**, *7*, 10465–10474.
46. Lauga, E.; DiLuzio, W. R.; Whitesides, G. M.; Stone, H. A. Swimming in Circles: Motion of Bacteria near Solid Boundaries. *Biophys. J.* **2006**, *90*, 400–412.
47. Toro-Sierra, J.; Tolkach, A.; Kulozik, U. Fractionation of α -Lactalbumin and β -Lactoglobulin from Whey Protein Isolate Using Selective Thermal Aggregation, an Optimized Membrane Separation Procedure and Resolubilization Techniques at Pilot Plant Scale. *Food Bioprocess Technol.* **2013**, *6*, 1032–1043.
48. O’Nuallain, B.; Shivaprasad, S.; Khetpal, I.; Wetzel, R. Thermodynamics of $\text{A}\beta$ (1–40) Amyloid Fibril Elongation. *Biochemistry* **2005**, *44*, 12709–12718.
49. Rühs, P. A.; Affolter, C.; Windhab, E. J.; Fischer, P. Shear and Dilatational Linear and Nonlinear Subphase Controlled Interfacial Rheology of β -Lactoglobulin Fibrils and Their Derivatives. *J. Rheol.* **2013**, *57*, 1003–1022.
50. Besseling, R.; Isa, L.; Weeks, E. R.; Poon, W. C. K. Quantitative Imaging of Colloidal Flows. *Adv. Colloid Interface Sci.* **2009**, *146*, 1–17.
51. Isa, L.; Lucas, F.; Wepf, R.; Reimhult, E. Measuring Single-Nanoparticle Wetting Properties by Freeze-Fracture Shadow-Casting Cryo-Scanning Electron Microscopy. *Nat. Commun.* **2011**, *2*, 438–438–9.